HIGHLIGHTED PAPER

Piezoelectricity regulated ohmic contact in M/$BaTiO_3$ (M = Ru, Pd, Pt) for charge collision and hydrogen free radical production in ammonia electrosynthesis

Shaoce Zhang [1], Dong Chen [1], Ying Guo [1], Rong Zhang [1], Yuwei Zhao [1], Zhaodong Huang [1,2], Jun Fan [1], Johnny C. Ho [1,*], Chunyi Zhi [1,2,3,4,*]

[1] Department of Materials Science and Engineering, City University of Hong Kong, 83 Tat Chee Avenue, Kowloon 999077, Hong Kong, China
[2] Hong Kong Center for Cerebro-Cardiovascular Health Engineering (COCHE), Shatin, NT, Hong Kong Special Administrative Region
[3] Centre for Functional Photonics, City University of Hong Kong, Kowloon, Hong Kong
[4] Hong Kong Institute for Clean Energy, City University of Hong Kong, Kowloon 999077, Hong Kong

Electrochemical nitrate reduction reaction (NO_3RR) is a promising alternative technique for NH_3 generation toward the energy-consuming Haber-Bosch process. Nevertheless, it remains hindered by the competitive hydrogen evolution reaction (HER). Herein, the piezoelectric effect of electron-rich $BaTiO_3$ with oxygen vacancies is introduced to promote NO_3RR performance. Combining with metal particles (Ru, Pd and Pt), the catalyst achieves a maximal Faradaic efficiency of 95.3% and NH_3 yield rate of 6.87 mg h^{-1} $mg_{cat.}^{-1}$. Upon piezoelectricity, the interface between metal nanoparticles and $BaTiO_3$ is effectively modulated from Schottky contact to ohmic contact, which leads to unobstructed electron transfer. Abundant hydrogen radicals (·H) can be then produced from the collision between plentiful electrons and polar water molecules adsorbed on the polar surface. Such ·H can significantly facilitate the hydrogenation of reaction intermediates in NO_3RR. Meanwhile, this process suppresses the Volmer-Heyrovsky step, therefore inhibiting the HER within a wide range of external potential. This work suggests a new strategy for promoting the performance of multi-electron-involved catalytic reactions.

Keywords: Electrochemical NO_3^- reduction; Piezoelectric effect; Ohmic contact; Charge collision; Hydrogen radicals

Introduction

Ammonia (NH_3) is an essential chemical as an indispensable feedstock in synthesizing nitrogen fertilizers and meanwhile regarded as a promising hydrogen-rich fuel [1–6]. Nevertheless, the Haber-Bosch route carried out to produce industrial-scale NH_3 currently consumes mass energy due to the requirement of high temperature and pressure, accompanied by releasing vast amounts of greenhouse gases [7–9]. Lately, aqueous-based electrochemical nitrogen reduction reaction (NRR) has attracted widespread attention as a potential alternative strategy, which can synthesize NH_3 from N_2 under mild conditions [10–14]. However, due to the high bond energy (940.95 kJ/mol) of N≡N, intensive competitive reaction of hydrogen evolution reaction (HER), and extremely low solubility of N_2 in solutions, the NH_3 yield rate is 2∼3 orders of magnitude inferior to that of Haber-Bosch process [15–19]. In contrast, nitrate (NO_3^-) ions, which are abundant in environmental pollutants as a nitrogen-containing alternative, could be decomposed into deoxidizing substances with comparatively low dissociation energy (204 kJ/mol) [20–22]. Therefore, electrochemical reduction of NO_3^- into NH_3 may contribute to solving both energy and environmental issues. The electrochemical nitrate reduction reaction (NO_3RR) associates a multi-electron and proton transfer process, which leads retarded kinetics and inevitably generates various byproducts such as NO_2^- and N_2H_4 [23–25]. Additionally, part of electron donors is meaninglessly consumed in HER, thus leading to

* Corresponding authors.
E-mail addresses: Ho, J.C. (johnnyho@cityu.edu.hk), Zhi, C. (cy.zhi@cityu.edu.hk).

 https://doi.org/10.1016/j.mattod.2023.03.011

an unsatisfactory NH_3 yield rate and Faradaic efficiency [26,27]. Typically, commonly used metal catalysts just manifest good NH_3 selectivity at low potentials but poor Faradaic efficiency at high potentials on account of severe hydrogen evolution competitive reaction [28,29]. Hence, it is fundamentally important to inhibit the competitive reaction and explore highly selective NO_3RR strategies.

Piezoelectric materials are featured by generating an internal polarization field under strain owing to the non-zero dipole moment, which is typically induced by the non-overlapping structure of the anion and cation centers. The materials can release a large number of piezoelectric charges, which availably adjust the charge distribution state and the amplitude of the depletion zone [30–32]. Since the conception of energy conversion utilizing piezoelectric zinc oxide nanowires was firstly proposed [33], piezoelectric catalysis has been studied by employing the characteristics of piezoelectric materials to realize the conversion from mechanical energy to chemical energy, as well as trigger and tune redox reactions [34–37]. This strategy possesses excellent potential in inducing catalytic behavior and boosting catalytic performance. For instance, the piezoelectric effect was adopted to enhance photocatalysis by introducing the polarization electric field to improve the separation of photogenerated carriers [38–41]. Meanwhile, as an intermediate layer, piezoelectric materials could promote the transfer of carriers at adjacent interfaces to improve catalytic performance [42]. These works verify the synergistic enhancement of multiple catalysis and expand the application of piezoelectric materials.

However, there are few research on the application and mechanism analysis of piezoelectricity in multi-electron-involved electrocatalytic reactions. Therefore, it is highly promising to employ the piezoelectric effects to improve the electrocatalysis performance of metal catalysts targeting a high selectivity and yield rate in the NO_3RR. In addition, the piezoelectric effect can adjust the contact state and the amplitude of the depletion zone, therefore regulating the electron transmission behavior. Accordingly, introducing more electrons can effectively take advantage of the modulation effect of piezoelectricity. Oxygen vacancies can act as donor doping and provide plenty of free electrons, which may facilitate catalytic performance [43–45].

Herein, we introduced the piezoelectric effect originating from electron-rich $BaTiO_3$ with oxygen vacancies (BTO-OV_x, x represents annealing time and x = 0.5 h, 1 h, and 2 h, corresponding to different concentrations of oxygen vacancies) to facilitate the electrochemical NO_3RR for NH_3 generation on metal (Ru, Pd, and Pt) catalysts. The piezoelectric polarization of BTO-OV_x nanocrystals under an ultrasonic environment could modulate the interface contact state, which could significantly reduce the electron transport barrier from BTO-OV_x to metal nanoparticles. A large number of electrons collide, which leads to the decomposition of the water molecules adsorbed on the polar interface during the transport process. This induces abundant hydrogen radicals (·H) and polar surface directly, which can boost the hydrogenation in the NO_3RR and suppress the Volmer-Heyrovsky step. With the ultrasonic excitation, the electrocatalysts maintain a remarkably weakened hydrogen evolution competitive reaction in a wide potential range and result in a substantial promotion in electrochemical NO_3RR, leading to superior NH_3 Faradaic efficiency (95.3%) and yield rate (6.87 mg h^{-1} $mg_{cat.}^{-1}$).

Results and discussion

As shown in the scanning electron microscope (SEM, Fig. S1a) and transmission electron microscope (TEM, Fig. S2a) images, the pristine BTO nanocubes possess a smooth surface. Notably, after introducing oxygen vacancies by vacuum heat treatment, the morphological characteristics and microstructures of the samples were well maintained (Fig. 1**a** and Fig. S1b), which is crucial to investigate the effect of oxygen vacancies on piezoelectric activity without other interferences. Compared with the pristine BTO in Fig. S2b, the high-resolution TEM (HRTEM) in Fig. 1**b** exhibits evident darkness in some regions, which is due to oxygen vacancies. Moreover, the lattice defects could be observed in the inverse fast-Fourier-transform images (the insets in Fig. 1**b**), which may originate from the oxygen vacancies [46]. Taking the BTO-OV_1 as an example, the Ru nanoparticles homogeneously distribute on the surface of the BTO-OV_1 particles, which is evidenced by Fig. 1**c** (SEM image is shown in Fig. S1c). The HRTEM image in Fig. 1**d** shows that Ru nanoparticles and BTO-OV_1 nanocubes are well crystallized. The measured lattice distances are 0.283 nm and 0.206 nm, corresponding to the (110) plane of BTO and (101) facet of Ru, respectively, which could be confirmed by the following X-ray diffraction (XRD) measurement. The seamless contacting heterostructures formed by the preferential crystalline orientations of the two crystals may promote electron transfer at the interface [40]. The spatial distribution of the Ti, Ba, O, and Ru elements in the Ru/BTO-OV_1 was revealed by scanning TEM (STEM) and energy dispersive spectroscopy (EDS) mapping images (Fig. 1**e**), confirming the homogenous loading of the Ru element on the BTO-OV_1 substrates. The crystal structures of the samples were then confirmed by XRD measurement (Fig. 1**f** and Fig. S3). The characteristic peaks of BTO, BTO-$OV_{0.5}$, BTO-OV_1 and BTO-OV_2 could be well indexed to tetragonal phase BTO (P4mm, JCPDS: 05-0626), which exhibits that the crystal structure with high crystallinity remains basically unchanged after being treated by vacuum heat. After the precipitation of Ru, the additional diffraction peak can be assigned to the (101) plane of hexagonal Ru crystals (P63/mmc, JCPDS: 06-0663).

Fig. 1**g** manifests the electron paramagnetic resonance (EPR) spectroscopy of the BTO-OV_x. All the samples demonstrate a similar signal (g = 2.002) produced by the electrons trapped in oxygen vacancies [47]. The signal intensity improves as the annealing duration prolongs, indicating the increase of the oxygen vacancy concentration. Furthermore, the ultraviolet–visible (UV–Vis) absorption spectra (Fig. S4a) were employed to confirm the effects of the oxygen vacancies. With the annealing time increasing, the absorption edge of the samples occurs redshift while the absorption intensity improves, which are typical manifestations of oxygen vacancies [48]. Correspondingly, a reduced band gap is exhibited in Fig. S4b (the details of the calculation are shown in supplementary information), confirming the existence of doping level due to the oxygen vacancies. The band structure of the samples was further investigated by ultraviolet photoelectron spectroscopy (UPS, hν = 21.22 eV, Fig. S5). The

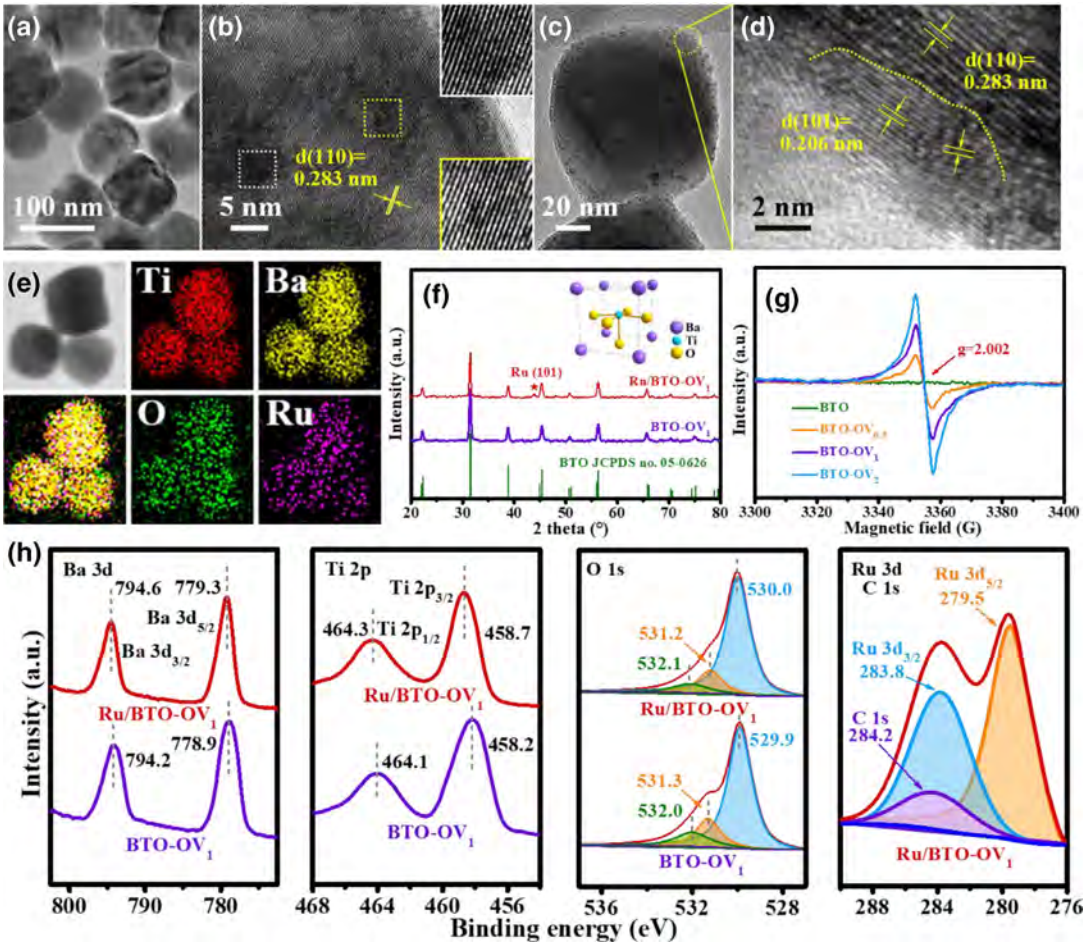

FIGURE 1

Characterizations of BTO-OV_1. (a,c) TEM and (b,d) HRTEM images of BTO-OV_1 and Ru/BTO-OV_1. The insets in (b) are inverse fast-Fourier-transform images of the corresponding areas. (e) STEM and EDS elemental mapping of Ru/BTO-OV_1. (f) XRD pattern of the samples. The inset shows the crystal structure of BTO-OV_1. (g) EPR spectra of BTO, BTO-$OV_{0.5}$, BTO-OV_1 and BTO-OV_2. (h) High-resolution XPS of Ba 3d, Ti 2p, O 1s and Ru 3d in Ru/BTO-OV_1.

work function (WF) was calculated by WF = hν-E_{cutoff}, in which E_{cutoff} signifies the secondary electron edge, and the valance band maximum (VBM) can be obtained through VBM = hν-(E_{cutoff} - E_{onset}) [49,50]. Combining with the band gap, the band positions of the samples are finally confirmed, and all the calculated results are summarized in Table S1. The results show that, as a donor doping, the oxygen vacancies supply abundant electrons and introduce a doping level nearby the conduction band. Moreover, the work function decreases with the vacancy concentration increases. The high electron density and low work function promote the transfer of electrons from the BTO-OV_x substrate to the metal particles, potentially reducing their activation barrier as catalysts [51]. Meanwhile, the X-ray photoelectron spectroscopy (XPS) spectra are shown in Fig. 1**h**, Figs. S6 and S7, in which the Ba $3d_{3/2}$ and $3d_{5/2}$ characteristic peaks at 794.2 eV and 778.9 eV are originated from Ba^{2+}, while Ti 2p peak is consist of $2p_{1/2}$ and $2p_{3/2}$ peaks of Ti^{4+} at 464.1 eV and 458.2 eV, respectively. The slight positive shift of these peaks after loading Ru nanoparticles could be attributed to the electron transfer from BTO-OV_1 to Ru, which is consistent with previous reports [52–54]. For instance, Ostojic et al. investigated that when Au_{147} is in contact with the $SnO_{1.9}$, the Au 4f peaks display a negative shift while the Sn 3d shows a positive shift, demonstrating the electron transfer from the $SnO_{1.9}$ to Au_{147} nanoparticles [54]. The O 1s peak could be deconvoluted into the peaks, which are assigned to the lattice oxygen (~529.9 eV), oxygen vacancies (~531.3 eV), and chemical-absorbed oxygen (~532.0 eV), respectively [55,56]. Moreover, the oxygen vacancy ratios are determined to be 6.90%, 12.32%, 16.87%, and 24.40% for BTO, BTO-$OV_{0.5}$, BTO-OV_1 and BTO-OV_2, respectively (Figs. S7c-f), which reveals the concentration of oxygen vacancy increase as the annealing duration prolongs. Except for the C 1s peak generated by carbonaceous impurities located at around 284.2 eV, the Ru 3d peak is composed of $3d_{5/2}$ (279.5 eV) and $3d_{3/2}$ (283.8 eV) peaks originating from metallic Ru with a spin-orbital splitting.

To verify the ferroelectricity of the as-prepared BTO-OV_1, Kelvin probe force microscopy (KPFM) was performed to intuitively understand the surface potential by examining the contact potential difference between the probe and the sample. As exhibited in the topography image (Fig. 2**a**), the nanoparticles hold a uniform distribution of sizes, which is in consistent with the SEM and TEM results. In Fig. 2**b**, the potential homogeneously distributes on the surface of BTO-OV_1 nanoparticles. This evidences that the polar surface adsorbs a large number of space-

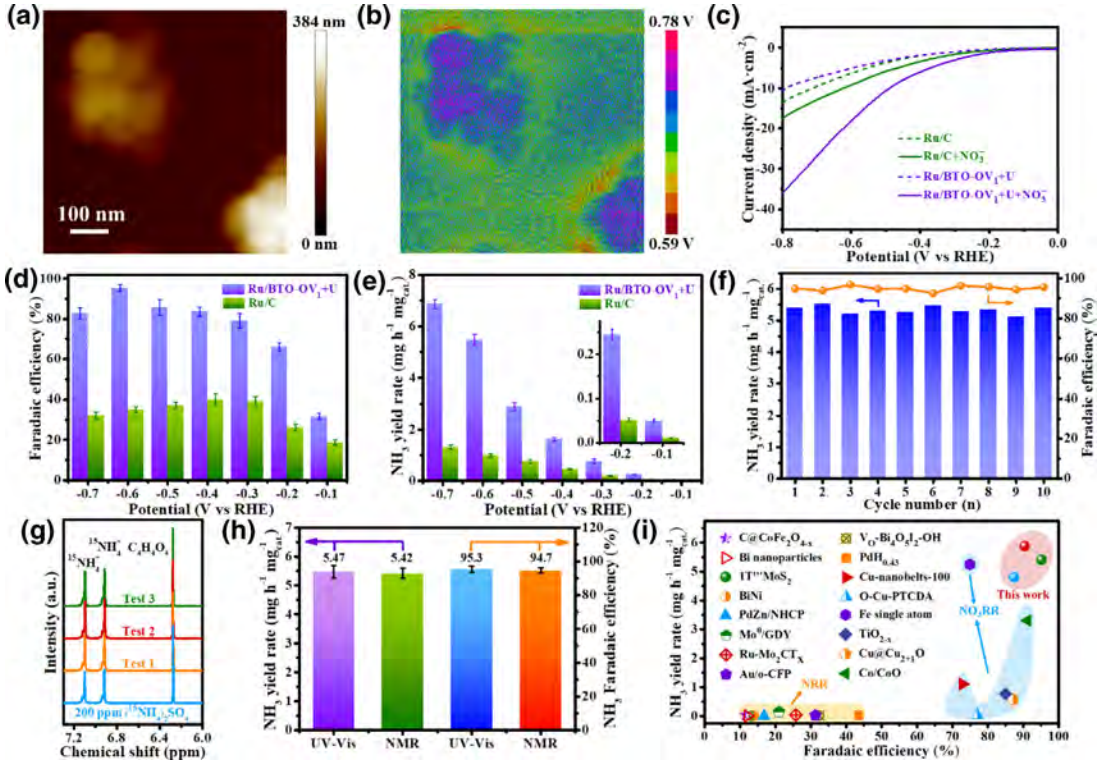

FIGURE 2

Ferroelectricity properties and piezo-electrocatalytic NO_3RR performances. (a) The atomic force microscope (AFM) topography image of BTO-OV_1. (b) KPFM image of BTO-OV_1 demonstrates the distribution of surface potential. (c) LSV curves of the samples. (d) NH_3 Faradaic efficiency and (e) yield rate of Ru/BTO-OV_1 + U and Ru/C. The inset in (e) is the yield rate at −0.1 V vs. RHE and −0.2 V vs. RHE. (f) The cycling stability test of Ru/BTO-OV_1 carried out at −0.6 V vs. RHE and each cycle takes 1 h. (g) ^1H NMR spectra of the electrolytes after the measurements and the referenced spectrum of $(^{15}NH_4)_2SO_4$. (h) The NH_3 yield rate and Faradaic efficiency of Ru/BTO-OV_1 + U measured by NMR and UV–Vis methods for a quantitative comparison. (i) Comparison of NH_3 Faradaic efficiency and yield rate between M/BTO-OV_1 + U and reported catalysts (NHCP is N-doped hollow carbon polyhedrons, GDY is graphdiyne, CFP is carbon fiber paper, V_o is oxygen vacancy and PTCDA is 3,4,9,10-perylenetetracarboxylic dianhydride).

free charges, confirming the excellent ferroelectric properties of the BTO-OV_1.

For evaluating the catalytic properties of the samples and determining the role of the piezoelectric effect, we investigated NO_3RR with a series of electrochemical measurements. The electrochemical active surface area (ECSA) was first proceeded based on the double-layer capacitance (Fig. S8), in which the Ru/BTO-OV_1 exhibits a slightly larger ECSA of 188.3 cm^2 than that of BTO-OV_1 (157.0 cm^2), verifying the increased electrochemical active sites. Besides, the linear sweep voltammetry (LSV) curves (Fig. 2**c**, Figs. S9 and S10) demonstrate that in the electrolyte containing NO_3^-, the Ru/BTO-OV_1 in ultrasonic circumstance (Ru/BTO-OV_1 + U) shows a larger geometric area- and ECSA-normalized current than that of the Ru/C within the measured range. Moreover, in Fig. 2**c** and Fig. S11a, when introducing NO_3^- in the electrolyte, the Ru/BTO-OV_1 + U reveals a more significant current increase than Ru/C and BTO-OV_1, manifesting a better NO_3RR selectivity. Furthermore, the current of Ru/BTO-OV_x (Fig. S11b) increases initially and then decreases as the annealing duration prolongs. This may result from that excessive oxygen vacancies could form a large number of defective dipoles. The excess dipoles can obviously pin the electrical domains and make it difficult for the domain walls to move in the material, leading to a suppressed catalytic performance [57]. On the basis of the LSV results, the time-dependent chronoamperometry (Fig. S12) measurement was carried out in an H-type cell, in which all the current densities at different applied potentials suggest favorable stability.

Then we quantified the generated products by UV–Vis spectrophotometry (Figs. S13-S15) to further evaluate the catalytic performance of the NO_3RR. As shown in Fig. 2**d and e**, the Ru/BTO-OV_1 + U achieves a maximum NH_3 selectivity of 95.3% at −0.6 V (Fig. 2**d**) with a yield rate of 5.47 mg h^{-1} $mg_{cat.}^{-1}$ (Fig. 2**e**). A gradual promotion of NH_3 yield rate occurs from the trace amounts at low potentials to a superior yield rate of 6.87 mg h^{-1} $mg_{cat.}^{-1}$ at −0.7 V vs. RHE, distinctly greater than that of Ru/C (1.31 mg h^{-1} $mg_{cat.}^{-1}$ at −0.7 V vs. RHE). The Ru/BTO-OV_1 + U also shows a smaller Tafel slope of 196 mV dec^{-1} (Fig. S16) than that of the Ru/C (256 mV dec^{-1}), verifying the faster reaction kinetics. Additionally, almost no hydrazine was detected in the byproducts of Ru/BTO-OV_1 + U and Ru/C samples (Figs. S15c and d). As for the other side reaction of NO_3^--to-NO_2^-, the Ru/BTO-OV_1 + U suggests a faster conversion of NO_2^--to-NH_3 (Fig. S17). Eventually, the total NO_3^- conversion efficiency (including NO_3^--to-NH_3, NO_3^--to-NO_2^- and NO_3^--to-N_2H_4) of Ru/BTO-OV_1 + U grows to 98.9% at −0.6 V vs. RHE (Fig. S18) along with the remaining Faradaic efficiency of 1.1% belongs to HER, indicating an observably restrained hydrogen evolution

competitive reaction compared to that of the Ru/C. This inhibition can be further verified in the test using electrolyte without NO_3^- (Fig. S19), in which Ru/BTO-OV_1 + U reveals a decreased current density (Fig. S19b), an enhanced Tafel slope (the inset in Fig. S19b), and a slower hydrogen evolution rate (Fig. S19c) compared with Ru/BTO-OV_1, directly manifesting that the piezoelectric effect suppresses the kinetic activity of HER in the system. For the NO_3RR performance of pure piezoelectric material BTO-OV_1 and BTO-OV_1 + U (Fig. S20), due to the participation of piezo-generated electrons induced by piezoelectric material BTO-OV_1 under an ultrasonic environment, the LSV (Fig. S20a) and NH_3 yield rate (Fig. S20c) reveal significant enhancement, but the ultrasonic environment has a negligible effect on the NH_3 Faradaic efficiency (Fig. S20b). This indicates that pure piezoelectric material without loading metal nanoparticles does not affect the selectivity of NO_3RR and highlights the necessity of studying their contact state. To confirm the enhancement may be contributed by the piezoelectric effect in essence rather than the influence of the ultrasonic environment, Ru/TiO_2 were manufactured by loading Ru nanoparticles on TiO_2 substrate without piezoelectric property. As shown in Fig. S21, a slight increase in LSV under an ultrasonic environment is observed due to the extra energy input but it is worth noting that there is no significant difference in NH_3 Faradaic efficiency. The performance of Ru/C (Fig. S22) under ultrasonic conditions was also evaluated (Fig. S23), which reveals similar trends to those of Ru/TiO_2 + U. This phenomenon demonstrates that this energy input has no effect on the selectivity of NO_3^--to-NH_3. However, for the reaction involving BTO-OV_1 with piezoelectric property, the Faradaic efficiency of Ru/BTO-OV_1 + U is significantly improved (Fig. S24), indicating that the performance enhancement in NO_3RR of Ru/BTO-OV_1 is attributed to the piezoelectric effect. Meanwhile, the NH_3 Faradaic efficiency and yield rate of BTO-OV_1 + U (Fig. S20d) and Ru/BTO-OV_1 + U (Fig. 2**f**) reveal fluctuation in each cycle but maintain overall stability in the cycling stability test, which indicates the favorable stability of the samples. To further confirm whether the ultrasonic environment could induce an influence on the structure and composition of the samples during the reaction, the morphological and chemical information of the used samples were studied. As shown in the TEM images of BTO-OV_1 and Ru/BTO-OV_1 after the cycling stability test with an ultrasonic environment (Fig. S25), there is no obvious change in morphology of the used samples compared with the fresh-made samples (Fig. 1**a and c**), indicates the structural stability of the samples. The STEM and EDS elemental mapping of Ru/BTO-OV_1 after reaction are also characterized (Fig. S26), in which Ru element shows a homogenous distribution on BTO-OV_1 substrates. Furthermore, the XPS analysis of the samples before (Fig. 1**h**) and after (Fig. S27) the reaction reveals that the valence states of each element in the sample remain unchanged. Consequently, we believe that the samples are stable under reaction conditions. Moreover, to confirm the universality of piezoelectric catalysis in improving the selectivity and yield rate in NO_3RR, the catalytic performance of Pd/BTO-OV_1 + U and Pt/BTO-OV_1 + U were evaluated (Fig. S28), in which both samples deliver improved NH_3 Faradaic efficiency and yield rate compared with the control samples. The NH_3 Faradaic efficiency of Ru/BTO-OV_1 also reveals a remarkable increase after introducing ultrasound in different pH environments including the electrolyte of 0.05 M H_2SO_4 and 0.1 M KOH (Fig. S29), further verifying the universality of the strategy.

To determine the nitrogen source in the conversion of NO_3^--to-NH_3, we employed ^{15}N-labeled NO_3^- as the feedstock and obtained the product at the maximum Faradaic efficiency potential (−0.6 V vs. RHE) to conduct an isotope labeling experiment by ^1H nuclear magnetic resonance (NMR) detection. As shown in Fig. 2**g**, the observed $^{15}NH_3$ characteristic peaks in the product spectra well correspond to the signals in the referenced spectra of $(^{15}NH_4)_2SO_4$. To control the errors, the independent electrolysis measurements of three samples were performed to calculate an averaged signal area. Combining with the calibration curve (Fig. S30), the $^{15}NH_3$ yield rate and Faradaic efficiency are finally recorded at 5.42 mg h^{-1} $mg_{cat.}^{-1}$ and 94.7%, in line with the UV–Vis results (Fig. 2**h**), testifying that the NH_3 is actually produced by nitrate electroreduction. To the best of our knowledge, the NH_3 yield rate and Faradaic efficiency of M/BTO-OV_1 + U (M = Ru, Pd, Pt) reported here are superior to previously reported works for N_2-to-NH_3 and NO_3^--to-NH_3 electroreduction in neutral media (Fig. 2**i**; Table S2).

To reveal the favorable piezoelectric effect of the as-prepared samples, the piezoresponse of Ru/BTO-OV_1 was intuitively detected by piezoresponse force microscope (PFM). The topography displayed in Fig. 3**a** is well consistent with the results in SEM and TEM of Ru/BTO-OV_1 nanoparticles. In the piezoelectric potential responsive image (Fig. 3**b**), the evident potential verifies that the nanoparticles produce a favorable piezoelectric response under pressure. Meanwhile, as shown in Fig. 3**c**, the piezoelectric properties of Ru/BTO-OV_1 nanoparticles are further revealed by piezoelectric hysteresis loops. The typical well-shaped butterfly loop is observed, and a variation of around 180° is testified in the phase angle, revealing the polarization switching characteristic and splendid piezoelectric properties of the sample [35,38]. In addition, we employ the finite element simulation to reveal the surface potential of Ru/BTO-OV_1 + U. Based on the ultrasonic cavitation, the ultrasonic waves trigger the vibration of a large number of minute bubbles in solution that eventually collapse, which could release a tremendous amount of energy and result in remarkable stress induced by the huge instantaneous pressure (≈10 MPa) on the immersed object surface. This effect can cause a remarkable piezoelectric potential in the BTO-OV_1 [58]. Hence, the pressure of 10 MPa is imposed on a BTO-OV_1 nanocube along the negative direction of the z axis during the COMSOL simulation. The results in Fig. 3**d** exhibit an obvious polar surface on BTO-OV_1 nanocube, manifesting a favorable piezoelectric polarization, which corresponds well to the PFM measurements.

In order to better verify the contribution of the piezoelectric effect in electrochemical NO_3RR, a field-effect transistors (FETs) device (Fig. S31) was fabricated to confirm the contact state between metal nanoparticles and BTO-OV_1. In the initial state, the I-V curve exhibits nonlinearity and asymmetry (Fig. 3**e**), demonstrating a Schottky contact at the interface [59,60]. As the pressure increases, the current of the device gradually rises and finally presents a linear symmetrical curve, manifesting a disappeared rectification characteristic. This phenomenon certifies that the height of the barrier can be tuned by the piezoelectric

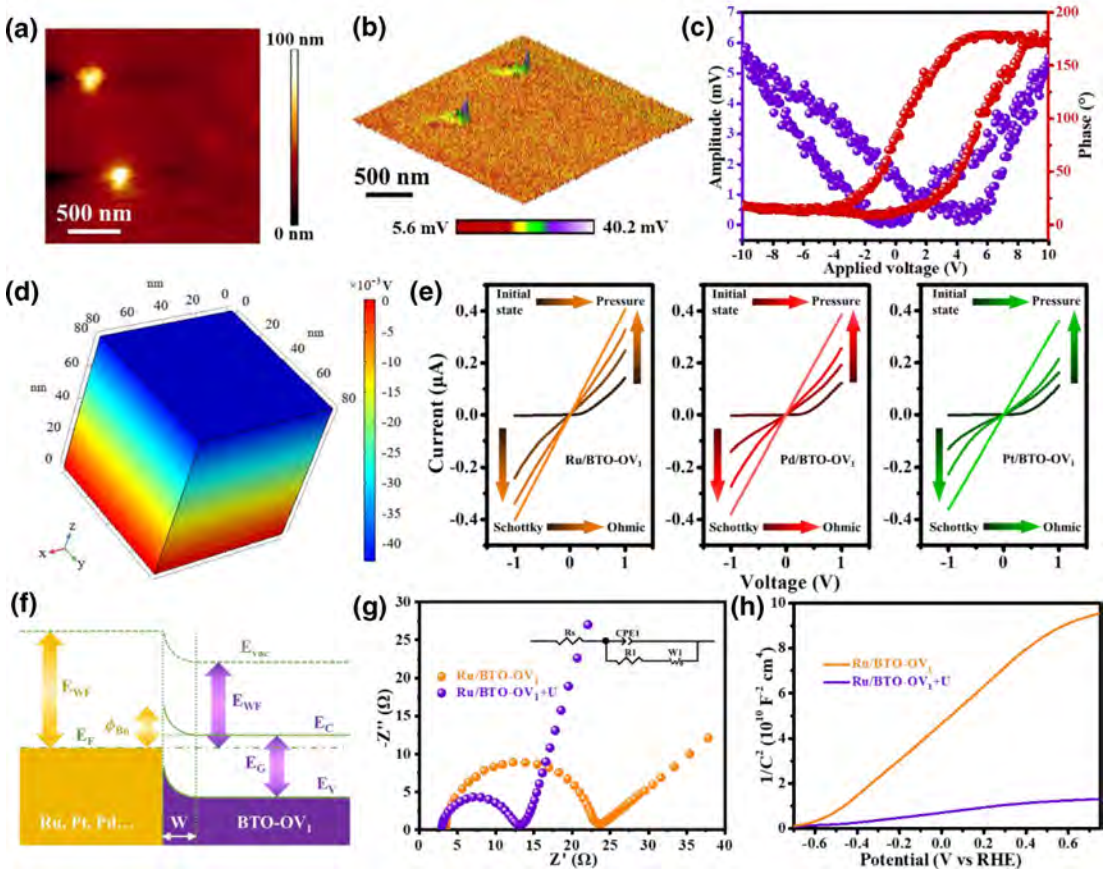

FIGURE 3

Piezoelectric properties and the effects of piezoelectricity on adjusting the contact state. (a) Morphology, (b) piezoelectric potential responsive images and (c) piezoresponsive phase (red) and amplitude curve (purple) of Ru/BTO-OV_1. (d) Potential distribution of BTO-OV_1 simulated by COMSOL. (e) I-V curves of M/BTO-OV_1 (M = Ru, Pd, Pt). (f) Energy band diagrams. E_{vac} and E_G are vacuum level and energy gap; E_{WF}, E_C and E_V are work function, conduction and valence band edge; E_F, W and ϕ_{Bn} are Fermi energy, depletion region and Schottky barrier. (g) Nyquist and (h) Mott-Schottky plots of Ru/BTO-OV_1 obtained with and without ultrasound. The inset of (g) is the equivalent circuit.

to change the contact state from Schottky contact to ohmic contact, which can be further proved by the following derivation and calculation. Since the conduction-band edge (E_C) is disturbed due to the piezoelectric charge, according to the energy band and electric field diagrams of M/BTO-OV_1 (M = Ru, Pd, Pt) interface (Fig. 3**f** and Fig. S32), the change in electric field intensity due to the presence of piezoelectric charges can be expressed as [61]:

$$E_p = -\frac{q\rho_p(W_p - x)}{\varepsilon_s}, \text{ for } 0 \le x \le W_p \quad (1)$$

where q is the unit electronic charge in absolute value and ε_s is the relative dielectric constant, ρ_p is the polarization charge density and W_p is the width of piezocharges. Then we define the barrier height when there is no piezoelectric charge as ϕ_{Bn0}. Due to the effect of piezoelectric charges, the change of potential distribution $\Delta\psi_i$ and Schottky barrier height can be written as

$$\Delta\psi_i = \frac{q\rho_p W_p^2}{2\varepsilon_s} \quad (2)$$

$$\phi_{Bn} = \phi_{Bn0} - \frac{q^2\rho_p W_p^2}{2\varepsilon_s} \quad (3)$$

This means that as the appearance of polarization charge density (ρ_p) due to triggering the piezoelectric effect, the barrier height (ϕ_{Bn}) can be reduced (Equation (3)). The piezopotential and barrier height could be adjusted by stress (induced by the pressure in our case), which is well revealed by the results of I-V curves shown in Fig. 3**e**.

The enhanced electric field intensity can effectively facilitate the transfer of charges. The electrochemical impedance spectroscopy (EIS, Fig. 3**g**, Fig. S33 and Table S3) was performed to demonstrate the charge transfer kinetics. The Nyquist plots were well fitted by the equivalent circuit in which R_s (corresponding to high-frequency intercept in the plots) represents a series resistance mainly including intrinsic resistance of electrodes and electrolyte resistance, R1 indicates the charge-transfer resistance, W1 is the Warburg impedance, and CPE1 is a constant phase element. Among the samples, the tests with ultrasound exhibit smaller semicircle diameters than those of control samples at

the range of medium frequency, indicating the enhanced charge transfer kinetics [62–64]. This can result from the adjusted barrier height and the enhancement of the electric field. At the low-frequency range, the linear curve reflects the Warburg diffusion process [65]. The samples manifest a greater slope under an ultrasonic environment, which is a characteristic of the rapid diffusion of ions to the electrode under the effect of an electric field. Furthermore, all Mott-Schottky plots (Fig. 3**h** and Fig. S34) present typical n-type positive slopes, and the charge density (N_d) can be obtained as [66]:

$$N_d = \frac{2}{e\varepsilon_0\varepsilon}\left[\frac{d\frac{1}{C^2}}{dV}\right]^{-1} \quad (4)$$

where e is the electron charge, ε_0 and ε are the vacuum permittivity and relative permittivity of the material, respectively, C is the capacitance of space charge, and V is the applied potential. The N_d values of M/BTO-OV_1 (M = Ru, Pd, Pt) are listed in Table S4, in which the charge concentrations measured under an ultrasonic environment are obviously higher than those of control samples, verifying the contribution of the piezoelectric effect on catalysis.

This phenomenon can be further testified based on the diffusion theory. Due to the n-type semiconductor characteristics of BTO, the carrier transmission in metal–semiconductor contact is mainly dominated by electrons. Therefore, the current could be expressed as [61]:

$$\boldsymbol{J} = \boldsymbol{J}_n = q\mu_n n\boldsymbol{E} + qD_n\frac{\mathrm{d}n}{\mathrm{d}x} \quad (5)$$

in which $\boldsymbol{J}_n$ represent the electron current density, μ_n and D_n are the mobility and diffusion coefficient of electrons, n is the concentration of free electrons, q and $\boldsymbol{E}$ are the unit electronic charge in absolute value and the electric field. Then, the solutions could be derived as [61]:

$$J_n \approx J_D\exp\left(-\frac{q\phi_{Bn}}{kT}\right)\left[\exp\left(\frac{qV}{kT}\right)-1\right] \quad (6)$$

in which J_D and ϕ_{Bn} are the saturation current density and the height of Schottky barrier, k, T and V are the Boltzmann constant, temperature and applied voltage. Therefore, defining J_D as J_{D0} when piezoelectric charges are absent and combined with Equation (3), the current could be expressed as

$$J_n \approx J_{D0}\exp\left(\frac{q^2\rho_p W_p^2}{2\varepsilon_s kT}\right)\left[\exp\left(\frac{qV}{kT}\right)-1\right] \quad (7)$$

In consequence, when the ϕ_{Bn} reduced owning to the introduction of the pressure in our system, the electron current density can be improved (Equation (6)). In other words, the increase of ρ_p can also improve the current density at the same time (Equation (7)). The polarization charge density could be changed by adjusting the degree of stress (induced by the pressure in our case), thus altering the total charge density in M/BTO-OV_1 (M = Ru, Pd, Pt).

Due to the regulated electron transmission behavior, the polar water molecules adsorbed on the polar surface collide with plentiful electrons and participate in the following chemical reaction [32].

$$e^- + H_2O \rightarrow OH^- + \cdot H \quad (8)$$

This process could generate abundant ·H, which can participate in hydrogenation in the NO_3RR process, and the existence of ·H is confirmed by EPR measurement utilizing the trapping reagent (5,5-dimethyl-1-pyrroline-N-oxide; DMPO). The time-dependent chronoamperometry was performed for 600 s in 0.1 M phosphate buffer solution (PBS) to achieve the dynamic equilibrium of ·H generation and quenching. In Fig. 4**a** and Fig. S35, the EPR results of the mixture including the electrolyte after reaction and DMPO exhibit nine characteristic signals belonging to two intensities with the ratio of 1:2. The hyperfine coupling constants further testify the existence of DMPO-H [67]. In the DMPO-involved EPR curves of the Ru/BTO-OV_1 + U performed electrocatalysis with a series of NO_3^- concentrations in 0.1 M PBS under argon environment (Fig. S35), the EPR peak intensity exhibits a weakening trend with the increase of NO_3^- concentration, which proves that ·H participates in the hydrogenation process of NO_3RR. Meanwhile, with a constant NO_3^- concentration (0.05 M), more intensive signals were detected as the ultrasonic intensity increased (Fig. 4**a** and Fig. S36), verifying an improved ·H concentration, which is attributed to that the collapse of more tiny bubbles triggers more piezoresponse. Then we recorded the variation of the current densities in NO_3RR with and without ·H trapping reagent of DMPO to further reveal the participation and promotion of ·H (Fig. 4**b**), in which all the NO_3RR currents at −0.6 V vs. RHE manifest significant decrease due to the consumption of ·H after introducing DMPO. As shown in the DMPO-involved current density (Fig. S37a) and EPR curves (Fig. S37b) measured in 0.1 M PBS, Ru/BTO-OV_1 + U exhibits a smaller current density and a stronger DMPO-H signal intensity, indicating the piezoelectric effect could suppress HER and induce abundant ·H through the collision effect. These results clearly demonstrate that abundant ·H directly participates in the hydrogenation reaction and facilitate the kinetics in electrochemical NO_3RR for NH_3 generation.

In addition to generating the ·H for boosting NO_3RR, the piezoelectric effect could enhance electron transfer and thus regulate the catalytic process, which is further understood by density functional theory (DFT) calculations. As shown in electron density difference mappings (Fig. 4**c** and Fig. S38), the Ru/BTO-OV_1 with pressure displays a stronger interaction between Ru and BTO-OV_1. Compared to the control sample, the enlarged electron density (red) around Ru could be conducive to the capture of electrons by the NO_3RR intermediate. Moreover, the free energy diagrams (Fig. 4**d** and Fig. S39) were plotted to further explore the mechanism during NO_3RR procedure. The process involves several deoxidation/hydrogenation reactions, which occurs following the route demonstrated in Figs. S40 and S41. *NO_3 is obtained by absorbing NO_3^-, and whereafter undergoes N-O cleavage, thus successively generating *NO_2, *NO, and *N, which is followed by protonation reactions to produce *NH, *NH_2, and *NH_3. Eventually, the *NH_3 desorbs to release NH_3. Specifically, for the rate-determining step (RDS) in NO_3RR from *NO_2 to *NO, the Ru/BTO-OV_1 with pressure displays an obviously decreased free energy difference ($\Delta G = 0.41$ eV to 0.07 eV), which indicates the promotion to NO_3RR by the piezoelectric effect.

Based on the experimental and theoretical calculations, the enhancement of piezo- electrocatalysis NO_3RR for NH_3 genera-

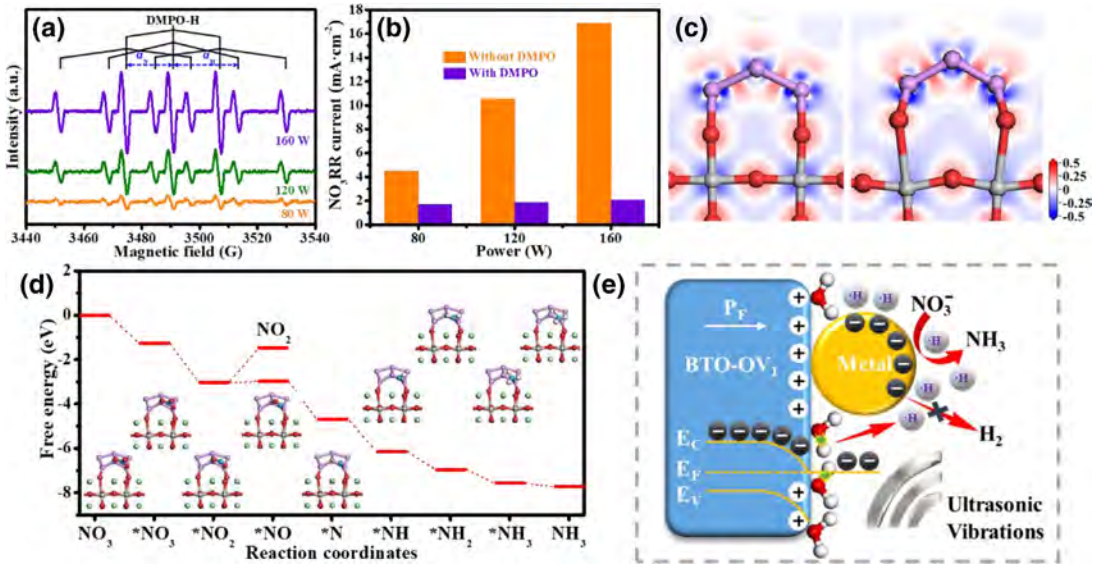

FIGURE 4

Generation of ·H and theory calculations. (a) EPR results of the mixture containing DMPO and electrolytes after 600 s reaction in 0.05 M NO_3^- and 0.1 M PBS under argon with various ultrasonic power (W), in which the hyperfine coupling constants $\alpha_N = 16.32$ G and $\alpha_H = 22.49$ G. (b) NO_3RR current density measured with the existence and absence of DMPO. (c) Electron density difference mappings of optimized Ru/BTO-OV_1 without (left) and with pressure (right). (d) The Gibbs free energy diagram of Ru/BTO-OV_1 in NO_3RR with pressure, in which the insets are the optimized structures of the intermediates adsorbed on Ru/BTO-OV_1. (e) The schematic diagram of electrochemical NO_3RR under ultrasonic environment. In (c) and (d), the gray, red, green, purple, blue and white spheres represent Ti, O, Ba, Ru, N and H elements.

tion is illustrated through a schematic diagram (Fig. 4**e**). With ultrasonic vibrations, ohmic contact appears at the interface, which could remarkably improve the charge transfer kinetics. Therefore, due to the built-in piezoelectric electric field, the larger work function of the metal particles [68,69], and the effect of the applied bias, plenty of electrons in the BTO-OV_1 rapidly transfer to the metal particles. The electrons collide with the water molecules, resulting in the direct generation of abundant ·H, which can directly participate in the hydrogenation reaction in the NO_3RR process and reduce the reaction barrier. On the other hand, the piezoelectric effect causes the modulation of the electron density, which is beneficial to the various intermediates adsorbed on the metal particles capturing the electrons, therefore reducing the free energy of the reaction, and realizing the improvement of NO_3RR performance. Meanwhile, the charge redistribution leads to the weakening of the *H adsorption on the surface of BTO-OV_1 and *H desorption on the surface of metal particles (Fig. S42). Since both too strong and too weak hydrogen adsorption ability is not conducive to the performance of HER, it shows that the piezoelectric effect is thermodynamically unfavorable for HER in this system [70].

Conclusion

In summary, the piezoelectric effect is firstly introduced to multi-electron-involved NO_3RR and demonstrated to be highly efficient in promoting the conversion of NO_3^--to-NH_3. Among the fabricated M/BTO-OV_1 (M = Ru, Pd, Pt), Ru/BTO-OV_1 + U exhibits impressive suppression to hydrogen evolution competitive reaction in a wide potential range and suggests a faster conversion of NO_2^--to-NH_3, achieving a superior NH_3 Faradaic efficiency of 95.3% and yield rate of 6.87 mg h^{-1} $mg_{cat.}^{-1}$. Furthermore, the favorable universality proved by improved selectivity of Pd/BTO-OV_1 + U and Pt/BTO-OV_1 + U electrocatalysts confirms the effectiveness of the piezoelectric effect on improving catalytic performance. The significant enhancement in NO_3RR performance originates from the adjustment of the barrier (from Schottky contact to ohmic contact) at the interface between BTO-OV_1 and metal particles due to the disturbance of piezoelectric charge, which boosts electrons to collide with polar water molecules, thus generating plentiful ·H directly to participate in the hydrogenation of reaction intermediates.

This work suggests a superior approach by employing the piezoelectric effect of electron-rich BTO-OV_1 to realize the conversion of mechanical energy to chemical energy and provides a novel strategy for inhibiting HER and improving electrochemical NO_3RR selectivity. Meanwhile, this idea of modulating electron transfer behavior is promising to be carried out in other catalytic processes designed for multi-electron-involved reactions, such as electrocatalytic reduction reaction of CO_2 and O_2, and hydrogenation of unsaturated aldehydes. Moreover, it will also be valuable to investigate other piezoelectric catalysis triggering modes widely existing in nature to promote practicability.

Data availability

Data will be made available on request.

CRediT authorship contribution statement

Shaoce Zhang: Conceptualization, Methodology, Investigation, Writing – original draft. **Dong Chen:** Methodology, Inves-

tigation, Writing – review & editing. **Ying Guo:** Methodology. **Rong Zhang:** Investigation. **Yuwei Zhao:** Investigation. **Zhaodong Huang:** Investigation. **Jun Fan:** Software, Formal analysis. **Johnny C. Ho:** Formal analysis. **Chunyi Zhi:** Conceptualization, Writing – review & editing, Funding acquisition.

Data availability

Data will be made available on request.

Declaration of Competing Interest

The authors declare that they have no known competing financial interests or personal relationships that could have appeared to influence the work reported in this paper.

Acknowledgements

This research was supported by GRF under the Project CityU 11212920.

Appendix A. Supplementary material

Supplementary data to this article can be found online at https://doi.org/10.1016/j.mattod.2023.03.011.

References

[1] G. Qing et al., Chem. Rev. 120 (2020) 5437–5516.
[2] Y. Ashida et al., Nature 568 (2019) 536–540.
[3] Z.Y. Wu et al., Nat. Commun. 12 (2021) 2870.
[4] W. He et al., Nat. Commun. 13 (2022) 1129.
[5] H. Liu et al., Angew. Chem. 134 (2022) e202202556.
[6] Y. Zhao et al., Nano Energy 97 (2022) 107124.
[7] G.-F. Chen et al., Nat. Energy 5 (2020) 605–613.
[8] H. Wang et al., J. Mater. Chem. A 10 (2022) 24462–24467.
[9] B.H.R. Suryanto et al., Nat. Catal. 2 (2019) 290–296.
[10] D. Yao et al., Chem. Eng. Sci. 257 (2022) 117735.
[11] Y. Guo et al., Adv. Energy Mater. 11 (2021) 2101699.
[12] D. Yao et al., Adv. Energy Mater. 10 (2020) 2001289.
[13] Y. Guo et al., Energ. Environ. Sci. 13 (2020) 2888–2895.
[14] J. Liang et al., Nano Res Energy 1 (2022) e9120010.
[15] Q. Hu et al., Energ. Environ. Sci. 14 (2021) 4989–4997.
[16] F. Wang et al., Small Struct. 2 (2021) 2000075.
[17] H. Cheng et al., Angew. Chem. 131 (2019) 15687–15693.
[18] Q. Liu et al., Small 18 (2022) 2106961.
[19] N. Zhang et al., ACS Nano 16 (2022) 4795–4804.
[20] N.C. Kani et al., Energ. Environ. Sci. 14 (2021) 6349–6359.
[21] Z. Deng et al., Mater. Today Phys. 28 (2022) 100854.
[22] W.J. Sun et al., Angew. Chem. Int. Ed. 60 (2021) 22933–22939.
[23] Y. Wang et al., J. Am. Chem. Soc. 142 (2020) 5702–5708.
[24] Z. Li et al., Mater. Today Phys. 23 (2022) 100619.
[25] Y. Guo et al., Energ. Environ. Sci. 14 (2021) 3938–3944.
[26] X. Deng et al., Adv. Sci. 8 (2021) 2004523.
[27] Y. Luo et al., J. Colloid Interface Sci. 629 (2023) 950–957.
[28] J. Li et al., J. Am. Chem. Soc. 142 (2020) 7036–7046.
[29] J.-X. Liu et al., ACS Catal. 9 (2019) 7052–7064.
[30] C. Pan et al., Chem. Rev. 119 (2019) 9303–9359.
[31] R. Su et al., Angew. Chem. Int. Ed. 58 (2019) 15076–15081.
[32] J.M. Wu et al., Adv. Mater. 28 (2016) 3718–3725.
[33] Z.L. Wang et al., Science 312 (2006) 242–246.
[34] Y.J. Chung et al., Adv. Energy Mater. 10 (2020) 2002082.
[35] H. You et al., Angew. Chem. 131 (2019) 11905–11910.
[36] R. Su et al., Angew. Chem. 133 (2021) 16155–16162.
[37] P. Zhu et al., Adv. Mater. 32 (2020) 2001976.
[38] P. Wang et al., Nano Energy 83 (2021) 105831.
[39] L. Pan et al., Adv. Energy Mater. 10 (2020) 2000214.
[40] S. Xu et al., Adv. Funct. Mater. 29 (2019) 1808737.
[41] S. Tu et al., Adv. Funct. Mater. 30 (2020) 2005158.
[42] X. Yu et al., Nano Energy 46 (2018) 29–38.
[43] S. Feng et al., Angew. Chem. 132 (2020) 2060–2064.
[44] Y. Li et al., Angew. Chem. 133 (2021) 923–929.
[45] S. Wang et al., Adv. Mater. 32 (2020) 2001385.
[46] S. Chen et al., Nat. Commun. 10 (2019) 788.
[47] J. Di et al., Adv. Energy Mater. 11 (2021) 2102389.
[48] H. Yu et al., Angew. Chem. Int. Ed. 58 (2019) 3880–3884.
[49] L. Liang et al., Joule 2 (2018) 1004–1016.
[50] J. Liu et al., Science 347 (2015) 970–974.
[51] T.-N. Ye et al., Nature 583 (2020) 391–395.
[52] H. Xu et al., Angew. Chem. Int. Ed. 57 (2018) 8654–8658.
[53] D. Gao et al., Adv. Mater. 34 (2022) 2108475.
[54] N. Ostojic et al., J. Am. Chem. Soc. 140 (2018) 13775–13785.
[55] X. Chen et al., Science 331 (2011) 746–750.
[56] H. Wang et al., J. Am. Chem. Soc. 140 (2018) 1760–1766.
[57] Y.C. Wang et al., Adv. Funct. Mater. 30 (2019) 1907619.
[58] E.B. Flint et al., Science 253 (1991) 1397–1399.
[59] H. Li et al., Nano Today 33 (2020) 100873.
[60] L. Zhao et al., Adv. Funct. Mater. 30 (2019) 1907999.
[61] Y. Zhang et al., Adv. Mater. 23 (2011) 3004–3013.
[62] G. Wang et al., Dalton Trans. 51 (2022) 9206–9212.
[63] G. Liang et al., Adv. Mater. 31 (2019) 1905873.
[64] P. Shen et al., J. Colloid Interface Sci. 629 (2023) 563–570.
[65] T. Butburee et al., Adv. Mater. 30 (2018) 1705666.
[66] S. Zhang et al., Nano Energy 79 (2021) 105485.
[67] J. Chen et al., Nat. Commun. 12 (2021) 3375.
[68] J. Shan et al., Adv. Mater. 31 (2019) 1900510.
[69] A. Meng et al., Adv. Mater. 31 (2019) 1807660.
[70] J. Greeley et al., Nature Mater. 5 (2006) 909–913.